Paper I

Parameterization of an iceberg drift model in the Barents Sea

Keghouche, I., Bertino, L. and Lisæter, K. A.

Journal of Atmospheric and Oceanic Technology, 2009, 26(10), 2216-2227

Parameterization of an Iceberg Drift Model in the Barents Sea

INTISSAR KEGHOUCHE, LAURENT BERTINO, AND KNUT ARILD LISÆTER

Mohn-Sverdrup Center/NERSC, Bergen, Norway

(Manuscript received 24 November 2008, in final form 7 April 2009)

ABSTRACT

The problem of parameter estimation is examined for an iceberg drift model of the Barents Sea. The model is forced by atmospheric reanalysis data from ECMWF and ocean and sea ice variables from the Hybrid Coordinate Ocean Model (HYCOM). The model is compared with four observed iceberg trajectories from April to July 1990. The first part of the study focuses on the forces that have the strongest impact on the iceberg trajectories, namely, the oceanic, atmospheric, and Coriolis forces. The oceanic and atmospheric form drag coefficients are optimized for three different iceberg geometries. As the iceberg mass increases, the optimal form drag coefficients increase linearly. A simple balance between the drag forces and the Coriolis force explains this behavior. The ratio between the oceanic and atmospheric form drag coefficients is similar in all experiments, although there are large uncertainties on the iceberg geometries. Two iceberg trajectory simulations have precisions better than 20 km during two months of drift. The trajectory error for the two other simulations is less than 25 km during the first month of drift but increases rapidly to over 70 km afterward. The second part of the study focuses on the sea ice parameterization. The sea ice conditions east of Svalbard in winter 1990 were too mild to exhibit any sensitivity to the sea ice parameters.

1. Introduction

Icebergs in the Barents Sea present a threat for navigation and offshore installations. The main source of icebergs in the Barents Sea are the Franz Josef Land archipelago glaciers, particularly the Renown glacier on Wilczek Land (Spring 1994). The Svalbard archipelago is the secondary source, particularly the Stonebreen glacier on Edgeøya. A smaller contribution of icebergs comes from glaciers of the northern tip of Novaya Zemlya. Observation campaigns during the Ice Data Acquisition Program (IDAP; Spring 1994) from 1988 to 1993 reported that icebergs have an average size of 91 m $\times$ 64 m $\times$ 15 m and a maximum observed size of 320 m $\times$ 279 m $\times$ 40 m. Although a great proportion of the icebergs stays and melts close to the calving area, icebergs can be found in more than half of the Barents Sea. Further, based on aerial surveys covering the period 1933–90, Abramov (1992) studied the seasonal cycle of the southern extension of the iceberg distribution. The southernmost extension is found to occur during January–May and the northernmost extension occurs during September–October. The interannual variability of the quantity and the geographical distribution of the icebergs depend on their calving rate and the wind. Predominantly northerly and northeasterly winds favor the southern extension of the icebergs.

Several studies in the Labrador Sea have successfully modeled the trajectories of icebergs by using forcing derived from observations (Smith and Banke 1983; Sodhi and El-Tahan 1980). Observations of ocean currents in the Barents Sea are largely insufficient for representing their complex dynamics. The lack of data has motivated us to use a coupled ice–ocean model to force the iceberg drift model. Bigg et al. (1997) produced a climatology of modeled iceberg trajectories over the Arctic by using a three-dimensional ocean circulation model and sea ice observations from Bourke and Garrett (1987). Lichey and Hellmer (2001, hereafter LH01) modeled the iceberg drift under the influence of sea ice in the Weddell Sea with a coupled ocean–sea ice circulation model. They focused on the relative importance of atmosphere, ocean, and sea ice forces that act on the iceberg drift in the Weddell Sea.

Following LH01, we adapt the model to the Barents Sea icebergs, which are much smaller than those in Antarctica. This has a consequence for drag force, because

Corresponding author address: Intissar Keghouche, Mohn-Sverdrup Center/Nansen Environmental and Remote Sensing Center, Thormoehlensgate 47, N-5006 Bergen, Norway.
E-mail: intissar.keghouche@nersc.no

DOI: 10.1175/2009JTECHO678.1

the form drag has a larger impact on trajectories of small icebergs. The model is configured to receive boundary conditions from the Towards an Operational Prediction System for the North Atlantic European Coastal Zones (TOPAZ) system (Bertino and Lisæter 2008). We study the parameterization of the iceberg drift model and focus on the dynamical forces that have the strongest impact on the iceberg trajectories as a first step toward forecasting the drift of icebergs.

The outline of this paper is as follows: section 2 provides a brief description of the model. Section 3 describes the dataset from the IDAP campaign that is used to evaluate our model system. Section 4 focuses on the sensitivity of the model to the mass of the iceberg and the ocean and atmospheric form drag coefficients. Section 5 describes the experiment testing the sea ice parameterization proposed by LH01. The work is discussed and summarized in section 6.

2. The model system

The iceberg drift model relies on the forcing components and their parameterization. Section 2a describes each forcing component: namely the ocean, atmosphere, and sea ice components. The implementation of the iceberg drift model is presented in section 2b.

a. Ocean and sea ice model

To model the ocean and sea ice, a version of the Hybrid Coordinate Ocean Model (HYCOM; Bleck 2002) is coupled to a dynamic sea ice model based on the elastic–viscous–plastic rheology by Hunke and Dukowicz (1997). The thermodynamic fluxes over open water, ice-covered water, and snow-covered ice are given in Drange and Simonsen (1996).

We used a one-way nested configuration that allows for high resolution and realistic boundary conditions in order to obtain a reasonable representation of the Barents Sea current system at limited computational cost. The large-scale model is a version of the TOPAZ3 forecasting system that covers the Atlantic and the Arctic Ocean and is run without data assimilation (Bertino and Lisæter 2008). The large-scale model provides boundary conditions to a regional model of the Barents and Kara Seas (Barents model). When nesting the slow boundary variables (i.e., baroclinic velocities, temperature, salinity, and layer interfaces), a simple relaxation technique is used. For the barotropic components (velocities and pressure), the boundary conditions are computed while taking into consideration both the waves propagating into the regional model from external solution and the waves propagating out through the boundary of the regional model (Browning and Kreiss 1982).

TOPAZ3 has an 11-km horizontal resolution in the Arctic with smooth transition toward lower resolution at the equator. Barents has a 4.5–5.8-km horizontal resolution. The model grids are created by using the conformal mapping algorithm of Bentsen et al. (1999).

Barents was initialized from the Generalized Digital Environmental Model, version 3 (GDEM3) climatology (Teague et al. 1990) and spun up for four years. The atmospheric forcing is from 6-hourly 40-yr European Centre for Medium-Range Weather Forecasts (ECMWF) Re-Analysis (ERA-40) data (see Uppala et al. 2005). The regional model includes tides, which are specified as a barotropic forcing at the open boundaries. The tidal data are taken from the Finite Element Solution tidal atlas 2004 (FES2004; Lyard et al. 2006).

An overview of the mean ocean currents for our focus area of the top 60 m during the period of study is shown in Fig. 1. With a model that does not resolve mesoscale activity for the region and the inaccuracy of its boundaries conditions, it is likely that residual currents are underestimated. Because the long-term average currents are weak in this region, it should not have a strong impact in this study. In addition, the sea ice edge is sharper and narrower in the sea ice model than in observations. Thus, the southern extension of low-concentrated sea ice is often underestimated in the model, but this should have minor impact on the iceberg trajectories.

b. Iceberg model

The iceberg model is based on LH01. The iceberg acceleration is proportional to the forces from the atmosphere $\mathbf{F}_{\mathrm{AT}}$, the water drag $\mathbf{F}_{\mathrm{W}}$, the Coriolis force $\mathbf{F}_{\mathrm{C}}$; the force resulting from the sea surface slope $\mathbf{F}_{\mathrm{SS}}$; and the force resulting from interaction with the sea ice cover $\mathbf{F}_{\mathrm{SI}}$:

$$M\frac{d\mathbf{u}}{dt} = \mathbf{F}_{\mathrm{AT}} + \mathbf{F}_{\mathrm{W}} + \mathbf{F}_{\mathrm{C}} + \mathbf{F}_{\mathrm{SS}} + \mathbf{F}_{\mathrm{SI}}, \tag{1}$$

where M is the iceberg mass and $\mathbf{u}$ is the iceberg velocity.

The atmospheric and oceanic forces act on the cross-sectional area above and below the water line, respectively, in a vertical plane as form drag and a horizontal plane as surface drag (Smith and Banke 1983). The atmospheric force is

$$\mathbf{F}_{\mathrm{AT}} = \left[\frac{1}{2}(\rho_a c_a A_{va}) + (\rho_a c_{da} A_{ha})\right]|\mathbf{v}_a - \mathbf{u}|(\mathbf{v}_a - \mathbf{u}). \tag{2}$$

The oceanic force $\mathbf{F}_{\mathrm{W}}$ is defined by the same quadratic drag law as $\mathbf{F}_{\mathrm{AT}}$ for each ocean model layer through the depth of the iceberg:

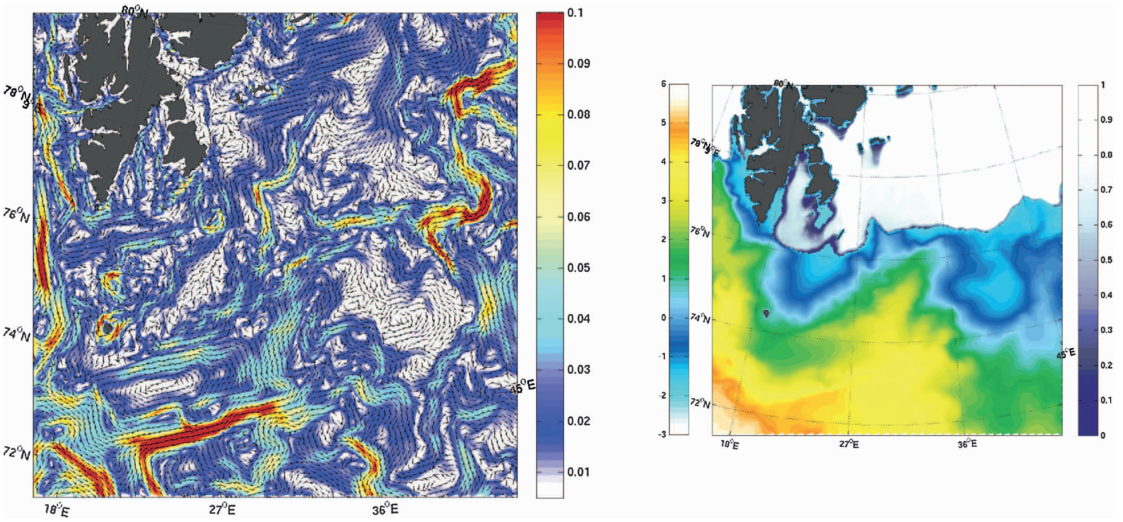

FIG. 1. (left) The modeled current vectors normalized over the top 60 m averaged from the last week of April to the second week of July 1990. Every second vector is represented. The background color is the current speed (m s^{-1}). (right) The modeled SST and sea ice concentration on 10 May 1990.

$$\mathbf{F}_{\mathrm{W}} = \sum_{i=1}^{n} \left\{ \frac{1}{2}[\rho_w c_w A_{vw}(i)]|\mathbf{v}_w(i) - \mathbf{u}|[\mathbf{v}_w(i) - \mathbf{u}] \right\} + [\rho_w c_{dw} A_{hw}(n)]|\mathbf{v}_w(n) - \mathbf{u}|[\mathbf{v}_w(n) - \mathbf{u}]. \quad (3)$$

In Eqs. (2) and (3), $\mathbf{v}_a$ and $\mathbf{v}_w(i)$ are the air and oceanic velocities, respectively; the index i is the ocean layer number; and n is the number of ocean layers in contact with the iceberg. The terms A_{va} and $A_{vw}(i)$ are the vertical cross-sectional areas in the air and water, respectively. The air and water densities are ρ_a and ρ_w are the air and water densities, respectively; c_a and c_w are the form drag coefficients; c_{da} and c_{dw} are the skin drag coefficients, set to 0.0022 and 0.0055, respectively, as in the sea ice model we use; and A_{ha} and $A_{hw}(n)$ are the horizontal areas of the iceberg in contact with the air and ocean layer n, respectively. If the surface drag area exceeds about 250 times the sail area of the iceberg, the surface drag becomes larger than the form drags (Smith and Banke 1983). For the relatively small lateral dimensions of Barents Sea icebergs, the form drag will be the most important factor.

The wind is assumed to be constant with height above sea level. However, the ocean currents vary with depth, as given by the ocean model. By tuning the air form drag coefficient, we can partly compensate for errors in the sail area and the variation of wind speed with height. In the same way, by tuning the water form drag coefficient, we partly compensate for errors in the keel area and inaccuracies in the ocean currents. Note that we do not vary c_w with depth, though internal wave drag might occur in the pycnocline (Smith 1993).

The third force acting on the iceberg is the Coriolis force,

$$\mathbf{F}_{\mathrm{C}} = 2M\Omega(\sin\phi)\mathbf{k} \times \mathbf{u}, \quad (4)$$

where Ω is the angular velocity of the earth, ϕ is the latitude, $\mathbf{k}$ is the unit vector perpendicular to the earth's surface, and $\mathbf{u}$ is the iceberg velocity. The force resulting from the sea surface slope is

$$\mathbf{F}_{\mathrm{SS}} = -M\mathbf{g}\sin\alpha, \quad (5)$$

where $\mathbf{g}$ is the acceleration due to gravity and α is the tilt of the sea surface slope estimated from the modeled sea surface height. The final force acting on the iceberg is due to interaction with sea ice. In LH01, the sea ice force depends nonlinearly on the sea ice concentration f; the sea ice strength P; a threshold P_s, above which the iceberg moves entirely with the sea ice; and the relative velocity of the iceberg with the sea ice,

$$\mathbf{F}_{\mathrm{SI}} = \begin{cases} 0 & \text{if } f \le 15\%, \\ -(\mathbf{F}_{\mathrm{A}} + \mathbf{F}_{\mathrm{W}} + \mathbf{F}_{\mathrm{C}} + \mathbf{F}_{\mathrm{SS}}) + \dfrac{d\mathbf{v}_{\mathrm{si}}}{dt} & \text{if } f \ge 90\% \text{ and } P \ge P_s, \\ \dfrac{1}{2}(\rho_{\mathrm{si}} c_{\mathrm{si}} A_{\mathrm{si}})|\mathbf{v}_{\mathrm{si}} - \mathbf{u}|(\mathbf{v}_{\mathrm{si}} - \mathbf{u}) & \text{otherwise,} \end{cases} \quad (6)$$

TABLE 1. Initial length H, width W, and height H (m); estimated mass (tons); and drifting period of the observed icebergs.

Buoy	L	W	H	Mass*	Initial position	Drifting period	Final position
7086	90	60	10	24300	78.11°N, 31.90°W	25 Apr–30 Jul	75.99°N, 25.13°W
7087	63	56	10	15876	78.07°N, 31.46°W	25 Apr–04 Jul	76.75°N, 26.62°W
7088	95	80	20	68400	78.92°N, 34.17°W	26 Apr–18 Jul	76.85°N, 29.68°W
7089	95	90	15	57712.5	79.03°N, 34.81°W	26 Apr–02 Jul	76.66°N, 32.10°W

* The mass is estimated for an idealized rectangular tabular iceberg with a depth of 4 times its height (Smith and Banke 1983).

where c_{si} is the sea ice coefficient of resistance set to 1, as in LH01 and A_{si} is the product of the ice thickness and the iceberg width. The sea ice strength P is a measure of the resistance of sea ice. It is defined by the standard formulation from Hibler (1979):

$$P = P^* h \exp[-C(1 - f)], \tag{7}$$

where f is the sea ice concentration and h is the sea ice thickness. The empirical constants P^* and C are set to 20 000 N m^{-2} and 20, respectively. This formulation makes the ice strength strongly dependent on the ice concentration and also allows the ice to strengthen as the thickness h increases. For regions of melting sea ice, P^* should ideally be reduced, but we did not change it for simplicity.

Previous iceberg drift modeling studies Sodhi and El-Tahan (1980) and Smith (1993) include a term proportional to the iceberg mass to simulate acceleration of water entrained in the wake of the iceberg (i.e., track of the waves left by the iceberg moving through the water). Here, this force is taken into consideration implicitly in the experiment by testing three different iceberg masses (section 4).

Smith (1993) discussed the effect of a wave radiation force but did not include it explicitly in his dynamical model, whereas Bigg et al. (1997) did. Because the form of the wave radiation force in Bigg et al. (1997) is proportional to Eq. (2), wind waves are present implicitly in the atmospheric force parameterization by selecting higher values for the air drag coefficient. This parameterization will not capture the effect of swells. Note that during the first month of the period of study, effects of waves are damped by the presence of sea ice.

To force the model, we used daily averaged ocean current fields from the HYCOM system described in section 2a and daily averaged wind fields from ERA-40. The tidal oscillations could have been represented by using hourly input, but they have been excluded to limit the size of the forcing dataset. We thus simulate residual iceberg drifts.

3. Iceberg observations

We focus on four specific icebergs on which Argos buoys were placed during late April 1990 under the IDAP program (Spring 1994). The available dataset consists of 17 reliable observed trajectories over the following three years: 1988 (seven), 1989 (five), and 1990 (six). All the icebergs were located in the northwestern region of the Barents Sea. During the years 1988 and 1989, the observed icebergs were mostly driven by inertial tidal oscillations and mesoscale activity, with the latter not being represented in the model. Furthermore, little information about the size of icebergs in 1988 was available. Therefore, we focus on data from 1990 where the time-averaged influence of the atmosphere and the ocean currents seemed to be the strongest. The observed sizes and recorded drifts of the icebergs are given in Table 1. The iceberg shapes are unknown, leaving a wide range of uncertainty in the mass and form drag coefficients of each iceberg. The 1990 iceberg trajectories are presented in Fig. 2. All the icebergs are located in the western Barents Sea. Hereafter, each iceberg is referred to by its Argos buoy number. Two icebergs, 1872 and 7085, were grounded for most of their recorded drift and were excluded from our study. The four remaining icebergs were subject to different regimes: initially within tightly packed sea ice and then in contact with open water. None of these icebergs was grounded. The recorded drift lasted 65, 70, 82, and 67 days for icebergs 7086, 7087, 7088, and 7089, respectively, starting one day earlier for the two southernmost icebergs (7086 and 7087).

Trajectories of the four icebergs are very similar during the first month, but they differ toward the end of the period. Each iceberg starts by following a clockwise loop and then moves mainly southwestward until late May.

The two northernmost icebergs have comparable trajectories until the end of the recorded drift. Both follow a southeastward trajectory until 21 and 19 June (for 7088 and 7089, respectively) and then move northwestward.

The two southernmost icebergs have more complex trajectories during the second month (see Fig. 3). Iceberg 7087 moves in a chaotic manner until 3 June and then moves northward until 14 June. It then follows an anticyclonic loop from 14 to 24 June and moves northwestward until the end of the record, 29 June. Iceberg 7086 follows two cyclonic loops from 1 to 13 June, then moves southward until 18 June, and moves northeastward until the end of its recorded drift. The diameter

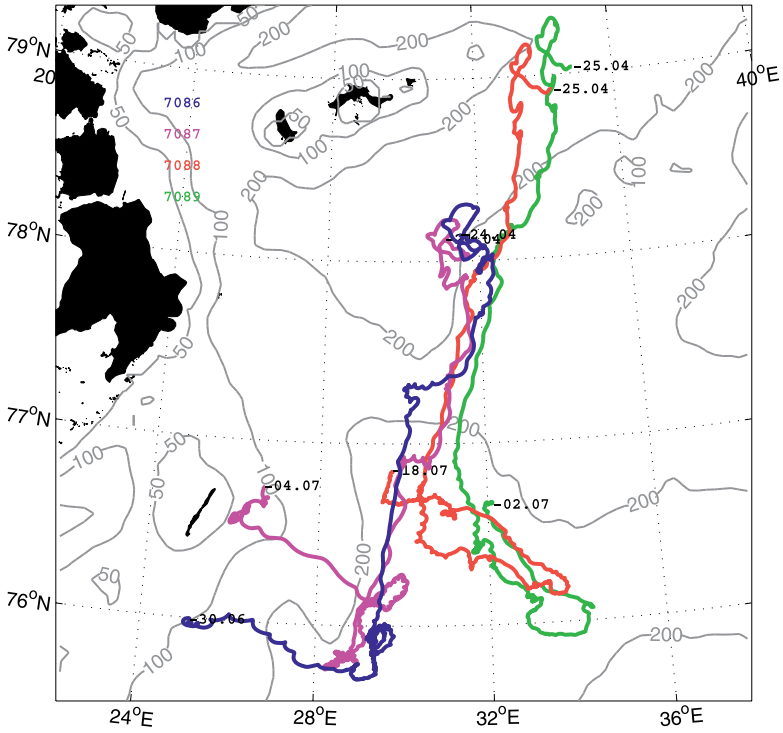

FIG. 2. Observed trajectories of four icebergs east of Svalbard from April to July 1990. Gray background contour lines are the isobaths at 50, 100, and 200 m.

and orbital period of the cyclonic loops correspond to typical eddy sizes in this area (Løyning 2001).

To select trajectories when the icebergs were within high concentration of sea ice, we used daily averaged sea ice maps from Special Sensor Microwave Imager (SSM/I) obtained with the Norwegian Remote Sensing Experiment (NORSEX) algorithm (Svendsen et al. 1983). The icebergs remained in areas where sea ice concentration was higher than 90% from their initial location until 17, 16, 20, and 24 May for icebergs 7086, 7087, 7088, and 7089, respectively.

4. Experiment 1: Sensitivity to iceberg mass and form drag coefficients

In this section, we measure the sensitivity of the model to uncertainties in the mass of the iceberg and the forcing by jointly varying the mass M, the ocean form drag coefficient c_w, and the atmospheric form drag coefficient c_a.

a. Setup

There is no information available regarding the shape of the icebergs being tracked. However, from statistics based on aerial stereo photography of 90 icebergs observed during 1990, most of the icebergs were tilting tabular (32%), pinnacled (31%), or tabular (16.7%; Spring 1994).

A tilting tabular iceberg is a tabular iceberg with its top surface no longer parallel to the ocean or sea ice surface. A pinnacled iceberg is an iceberg with a central spire or pyramid, with one or more spires. The only information we have from each iceberg is its initial length, width, and height. We chose to consider three different possible iceberg shapes in our simulations that would change the icebergs mass M but not the cross-sectional areas A_{va} and $A_{vw}(i)$ in contact with the winds and ocean currents, respectively. We assume a tabular iceberg with the shape of a rectangular prism and a sail area equal to the product of the observed width and height. It will be referred to an iceberg with mass 100%M. An iceberg with a triangular prism shape, with the same A_{va} and $A_{vw}(i)$ as the tabular iceberg has a mass of 50%M. Finally, the last experiments with icebergs defined as 35%M could correspond to an eroded iceberg with one large vertical wall. This way of changing the iceberg mass is a crude way of taking into account the geometrical configuration of the iceberg.

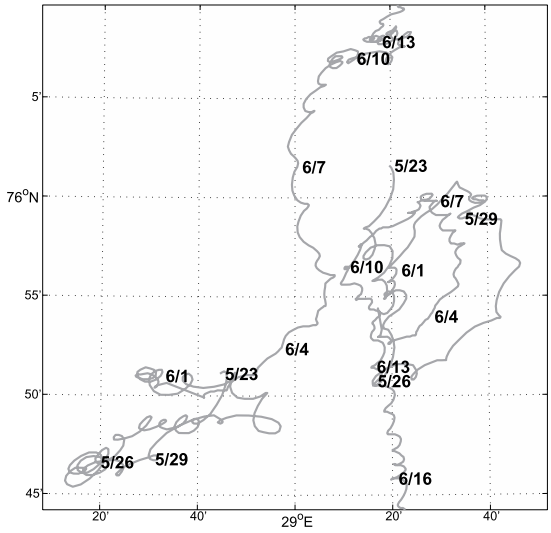

FIG. 3. Zoom on a part of the observed trajectory of icebergs (left) 7087 and (right) 7086. The date (month/day) is indicated for every third day.

The values of c_a and c_w are sampled, as in Table 2. Because we focus on the ocean and atmospheric drag in this experiment, the sea ice force is defined as a regular drag relationship independent of P:

$$\mathbf{F}_{\mathrm{SI}} = \begin{cases} 0 & \text{if} \quad f \le 15\%, \\ \frac{1}{2}(\rho_{\mathrm{si}} c_{\mathrm{si}} A_{\mathrm{si}})|\mathbf{v}_{\mathrm{si}} - \mathbf{u}|(\mathbf{v}_{\mathrm{si}} - \mathbf{u}), & \text{otherwise.} \end{cases} \tag{8}$$

MEASURE OF THE ERROR IN THE MODELED ICEBERG DRIFT TRAJECTORIES

The performance of each experiment is analyzed by measuring the geographical distance between modeled and observed iceberg drift and by counting the successful simulations for different values of the parameters. The errors in the distance should increase with time as a result of unresolved ocean and atmospheric circulation processes and parameterization errors. Consequently, we define a linearly decreasing weighting function of time so that the earlier part of the trajectory counts more than the later part:

$$\Delta d = \frac{1}{2m(m+1)} \sum_{t=1}^{m} (m - t)\epsilon(t), \tag{9}$$

where m is the number of time iterations, t is the time iteration, and $\epsilon(t)$ is the geographical distance between the observed iceberg and the modeled iceberg at time t.

TABLE 2. Parameter ranges for expt 1. Tested values for the mass, the atmospheric form drag coefficient c_a, and the oceanic form drag coefficient c_w for the four icebergs with sea ice force defined as in Eq. (8).

Mass (%)	100, 50, and 35
c_a	from 0.1 to 2.0; every 0.1
c_w	from 0.05 to 1.0; every 0.05

We apply this method over the whole drifting period to evaluate the modeled trajectories of the four icebergs and store the best ones into classes of distances.

b. Results

Sections 1 and 2 present a qualitative comparison between modeled and observed trajectories for the "full" mass experiment, 100%M. We obtained similar results with the 50%M and 35%M experiments (not shown). Further, section 3 highlights the relation between the optimal form drag coefficients and the mass. For the two northernmost icebergs, 7088 and 7089, the best ensemble runs have mean weighted distances less than 20 km. For the two southernmost icebergs, 7086 and 7087, the best ensemble runs have mean weighted distances less than 30 and 35 km, respectively.

1) TRAJECTORIES

The best trajectories for each iceberg are shown in Fig. 4. The two northernmost modeled icebergs (7088 and 7089) closely follow the observations over the entire drifting period. The best members remain, on average, within 20 km of the observed icebergs over the entire recorded drift.

For the two southernmost icebergs (7086 and 7087), modeled and observed trajectories diverge after the first month. Nevertheless, we point out that even if the modeled trajectory did not reproduce features from 26 May to 26 June, the drift patterns in the last part of the trajectory (3 days for 7086 and 5 days for 7087) are parallel to the observed ones. The best members remain within 25 km, on average, over the first half of the trajectory of the observed icebergs and within 45 km over the entire trajectory.

2) RELATIVE CONTRIBUTION OF FORCES

An evaluation of the contribution of each forcing component for each iceberg drift period highlights the importance of the three main forcing components: the wind forcing, the oceanic forcing over the drift of the iceberg, and the Coriolis force (see Fig. 5). The forces due to sea ice and sea surface slope are negligible for this simulation. Figure 6 shows how the position errors and the spread of the successful runs increased with time.

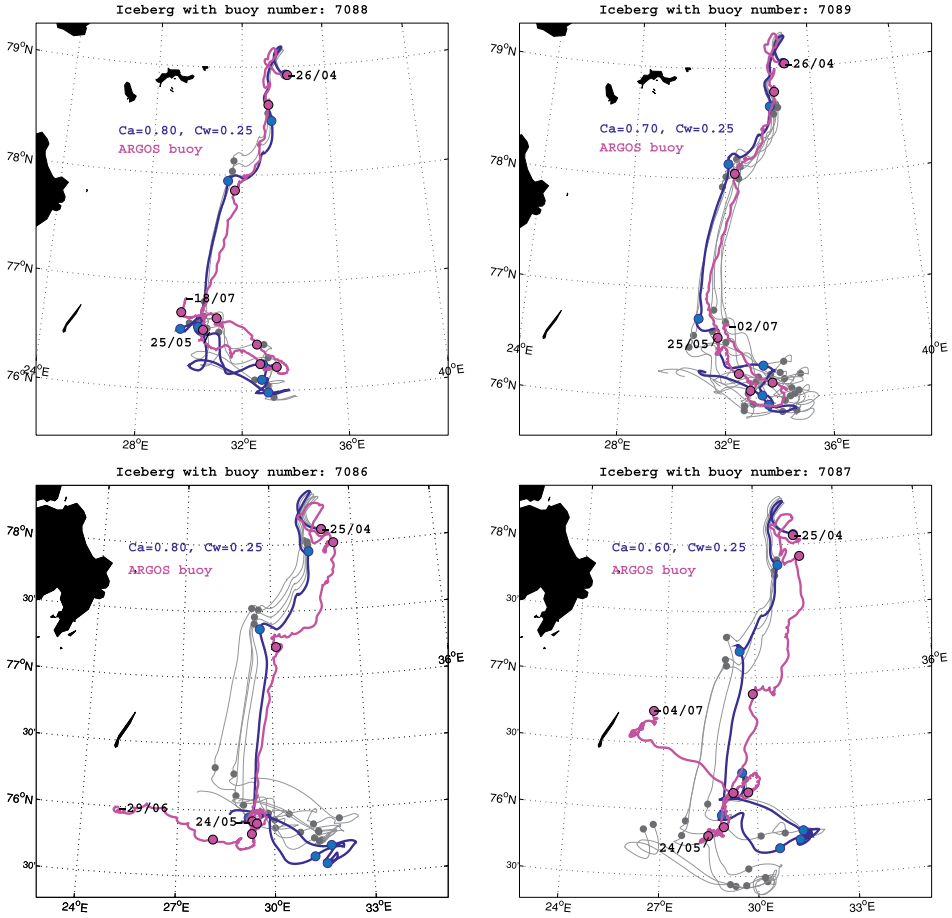

FIG. 4. Best modeled iceberg trajectories, when considering the icebergs as rectangular prisms, are shown in gray and blue. The blue trajectory is the one with the minimum mean weighted distance from the observations. The observed trajectory is given in magenta. Filled circles are plotted for every tenth day.

The exception is the period from 27 May to 5 June, the time when the two southernmost icebergs (7086 and 7087) were subject to forces that the model does not represent.

3) Optimal mass and form drag coefficients

Tuning the ocean and air form drag coefficients allows for a calibration of the modeled iceberg trajectories to the observed ones. These coefficients represent uncertainties related to the shape of the iceberg and uncertainties in the forcing fields: namely, the ocean and sea ice model and atmospheric data. Smith (1993) modeled short (from 11 to 73 h) iceberg trajectories off the east coast of Canada by using wind and current from nearby observations. He found little improvement by tuning the iceberg parameters. In our case, the parameterization is more critical, because trajectories are simulated over a much longer period and the modeled forcing fields have larger errors.

The successful model runs are presented in Fig. 7 as scatterplots of drag coefficients for three different iceberg mass experiments. For each experiment, there is an optimal range of values (c_w, c_a); as the mass increases, so do the optimal (c_w, c_a) values. In addition, the range of optimal values is broader for bigger icebergs. This is because a small change in c_w or c_a has a stronger impact on small icebergs and the effect of Coriolis force is larger on large icebergs. By linking the three clouds together with a linear regression, we found slopes of 0.35, 0.32, 0.31, and 0.29 for icebergs 7089, 7088, 7087, and 7086, respectively. These values represent the optimal ratio

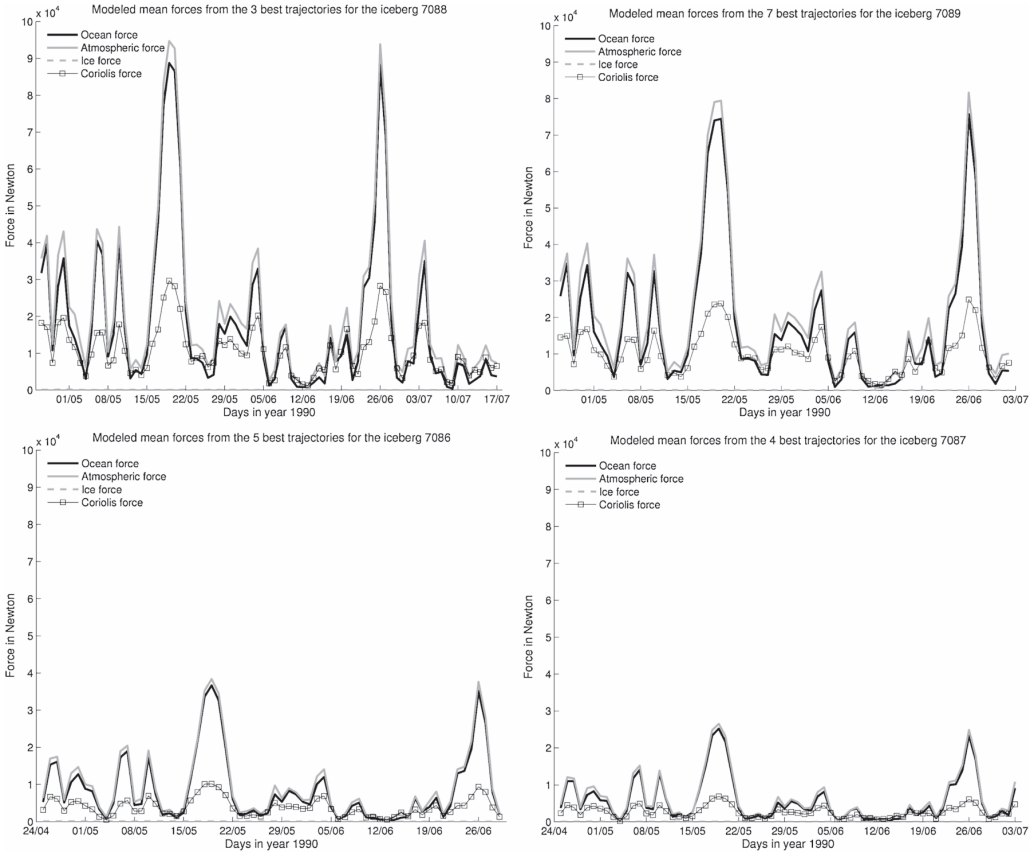

FIG. 5. Daily mean amplitude of the ocean, atmosphere, and ice force components for the best ensemble over the entire drifting period of all icebergs.

between c_w and c_a in our model, which is independent of the mass. The relation between the optimal c_w and c_a and the iceberg mass M is apparently linear. A linear relation is expected, considering the very small impact of $\mathbf{F}_{SS}$ and $\mathbf{F}_{SI}$ on the iceberg motions in our simulation. One can therefore assume the simplified force balance

$$\mathbf{F}_{\tilde{A}} + \mathbf{F}_{\tilde{W}} = -\mathbf{F}_C, \tag{10}$$

where $\mathbf{F}_{\tilde{A}}$ and $\mathbf{F}_{\tilde{W}}$ are the atmospheric and oceanic forces, respectively, with each neglecting the horizontal friction. Considering the mean ocean velocity $\mathbf{v}_w$ across the iceberg drift and A_{vw} as the vertical area of the iceberg, then

$$\mathbf{F}_{\tilde{A}} = \frac{1}{2}(\rho_a c_a A_{va})|\mathbf{v}_a - \mathbf{u}|(\mathbf{v}_a - \mathbf{u}) \quad \text{and} \tag{11}$$

$$\mathbf{F}_{\tilde{W}} = \frac{1}{2}(\rho_w c_w A_{vw})|\mathbf{v}_w - \mathbf{u}|(\mathbf{v}_w - \mathbf{u}). \tag{12}$$

If we assume known velocities at time t and a linear relation between c_w and c_a, we obtain the following relation between the mass M and c_a:

$$(c_a + Kc_a)\mathbf{D} = M\tilde{\mathbf{C}}, \tag{13}$$

where K is constant, $\mathbf{D}$ is the drag forces divided by the drag coefficients, and $\tilde{\mathbf{C}}$ is the Coriolis force divided by the mass.

Under these simplified assumptions, the relationships between, M, c_w, and c_a are linear. Also note that, as M increases, c_w and c_a increase accordingly, which explains the clustering of high (low) c_a and c_w values with high (low) mass M.

5. Experiment 2: Influence of the sea ice strength

In this section, we evaluate whether the parameterization of the sea ice forcing (e.g., for the large Weddell

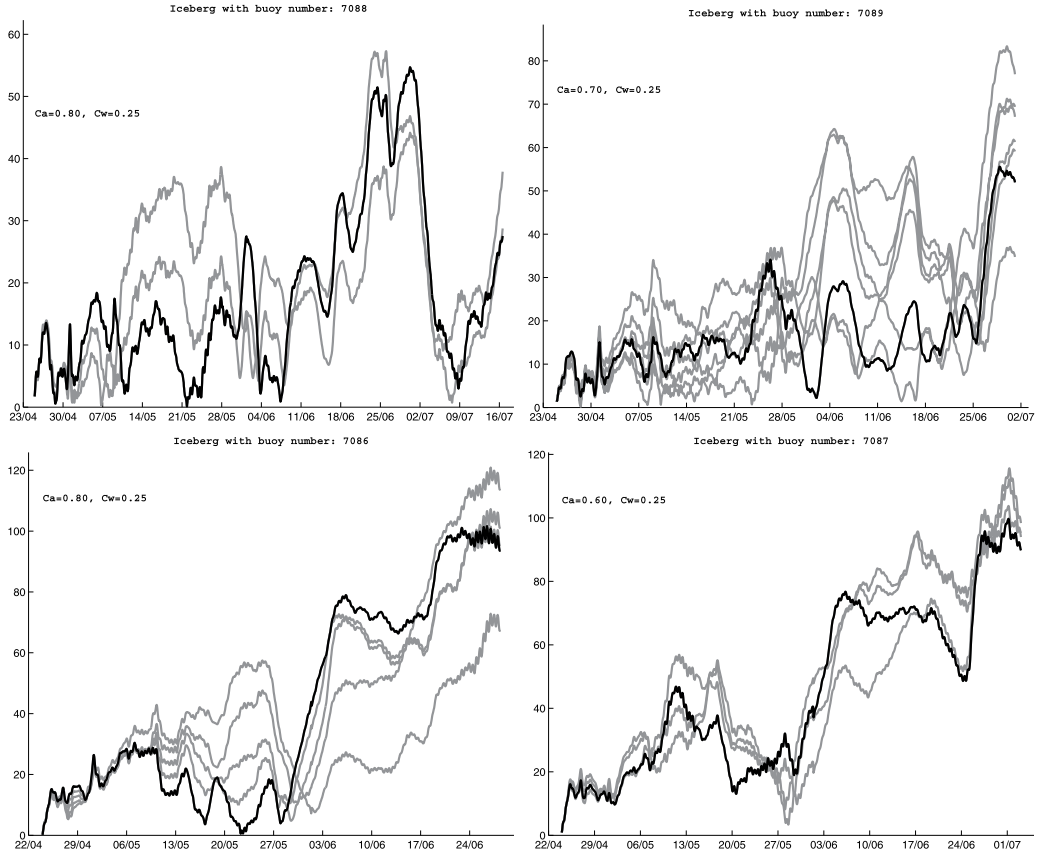

FIG. 6. Hourly distances (gray) between the successful runs and the four observed icebergs. The black line is the best modeled run with the minimum mean weighted distance.

Sea icebergs) in LH01 is applicable to the much smaller icebergs in the Barents Sea.

a. Setup

Calculated sea ice strength from the sea ice model shows that, during late winter 1990, the sea ice strength was rather weak in the western Barents Sea, less than 6500 N m^{-1} most of the time from late April to July. This motivated the choice of the sampling of P_s shown in Table 3. Note that the maximum sea ice strengths along all the modeled trajectories are 3721.5, 3779.9, 5980.33, and 6530.0 N m^{-1} for icebergs 7086, 7087, 7088, and 7089, respectively. We consider here only tabular icebergs with 100%M. Infinity corresponds to the experiments when the P_s parameterization is not used [i.e., $\mathbf{F}_{\mathrm{SI}}$ is defined by Eq. (8)].

For $P_s = 1000$ N m^{-1}, the minimum ice thickness able to lock an iceberg in the sea ice is 0.37 m when the sea ice concentration f is 90% and 0.05 m when f is 100%, which is less than the typical ice thickness encountered in the Barents Sea. Hence, with $P_s = 1000$ N m^{-1}, the icebergs will tend to follow the movement of sea ice. For $P_s = 6500$ N m^{-1}, the corresponding minimum ice thickness is between 2.4 and 0.325 m. In this case, icebergs will at times move with sea ice, but other times not. As in LH01, shear and bending forces that occur because of iceberg tilt and rotation are neglected, which means that sea ice forces may be underestimated.

MEASURE OF THE ERROR IN THE MODELED ICEBERG TRAJECTORIES

Because the later parts of the trajectories are in low-concentrated sea ice, the parameterization of P_s has little influence on the icebergs. We therefore restrict the optimization to the first 10 days of drift. Only trajectories with a mean distance to the observations of less than 15 km are retained. To focus on the effect of the P_s parameterization, we need to remove the bias in the

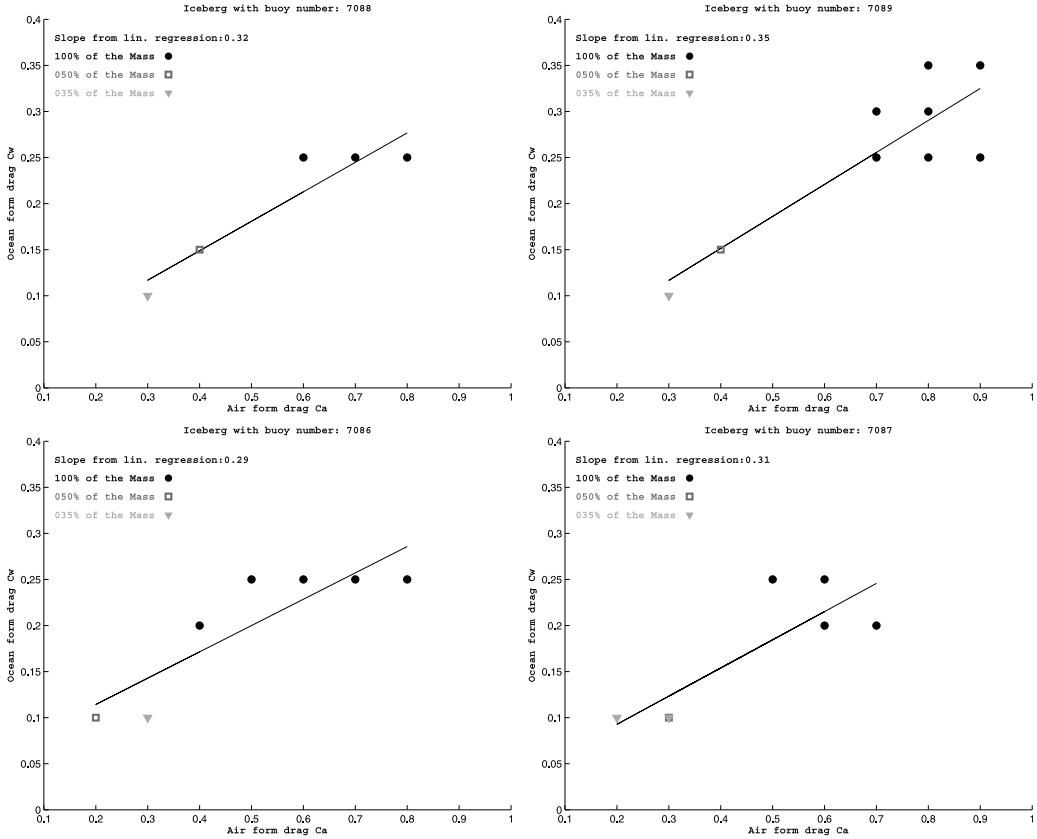

FIG. 7. Scatterplots of the ocean drag coefficients against the air drag coefficient for the successful experiments with three different masses.

modeled trajectory that comes from uncertainties of c_w and c_a. Consequently, we make a first selection of trajectories keeping only the successful (c_w, c_a) couples for each iceberg, as obtained from experiment 1.

b. Results

From the histograms (Fig. 8), the proportion of representative trajectories with no P_s parameterization [i.e., $\mathbf{F}_{SI}$ defined in Eq. (8)] is comparable to the others for the two southernmost icebergs. For the two northernmost icebergs, the best simulations are given by experiments with no P_s parameterization and experiments with P_s = 6500 N m^{-1}. Thus, there is no evidence that the P_s parameterization is significantly better for the four icebergs studied. However, sea ice characteristics have strong interannual variability in the area. The year 1990 was not particularly severe, and the sea ice can be thicker during other years. Though the proportion of multiyear ice is usually small in the western Barents Sea, it can be important in the eastern Barents Sea. Therefore, the sea ice force, as specified in Eq. (6), should not be excluded for an iceberg drift model in the Barents and Kara Seas. According to our experiments, a P_s value of 13 000 N m^{-1}, as in LH01, remains acceptable despite the fact that Barents Sea icebergs are about 10 times smaller than the ones in the Weddell Sea. Thus, the iceberg would be locked into sea ice only for more severe sea ice conditions than in our experiments.

6. Discussion and conclusions

This study focuses on the parameter estimation of an iceberg drift model in the Barents Sea. Four icebergs drifting southeast of Svalbard observed for more than two months in 1990 have been modeled. The simulations have a precision better than 20 km during the two months of drift of the two northernmost icebergs and better than 25 km during the first month of drift for the two others. For the latter two icebergs, although they are only about 100 km south of the two northernmost at the

TABLE 3. Parameter range for expt 2. Tested values for the sea ice strength threshold value P_s, the atmospheric form drag coefficient c_a, and the oceanic form drag coefficient c_w for the four icebergs considered rectangular prisms (100%M).

P_s (N m^{-1})	1000, 3000, 4500, 6500, and ∞
c_a	from 0.1 to 2.0; every 0.1
c_w	from 0.05 to 1.0; every 0.05

beginning, unpredicted circumstances such as melting, unresolved mesoscale features in the forcing, or a sudden change of shape and mass make the model error increase rapidly to 70 km in the second month.

In the first experiment, we sampled the iceberg masses and the atmospheric and ocean drag coefficients. The cross-sectional area of the iceberg was kept constant, whereas the ice mass was increased as a crude way of changing the geometry of the iceberg.

We found a common ratio of c_w to c_a between 0.29 and 0.35, independently of the chosen geometry. The ratio between the optimal atmospheric and ocean drag components is similar across the experiments, though we have little information about the geometry of the icebergs. Furthermore, the fact that the two southernmost icebergs have a much broader range of optimal c_w and c_a values highlights either some uncertainty in the chosen geometric configuration over the first month of integration, or it indicates that melting has been important for those two icebergs toward the end of the iceberg drift period.

As the iceberg mass increases, so do the optimal atmospheric and ocean form drag coefficients. A simple force balance between drag forces and the Coriolis force explains this linear behavior. The relation between optimal drag coefficients and the iceberg mass highlights the importance of the iceberg geometric configurations when modeling the trajectories. A value of (c_w, c_a) that provides the best trajectory for an iceberg of mass M may yield to a significantly different trajectory if the mass is 50%M, given that their cross-sectional area is the same. In a similar manner, the initial determination of the mass of the iceberg is important for successful modeling of their trajectories. In further studies, the ocean and atmospheric form drag should be a function of the iceberg mass.

It must be stressed that the optimal form drag factors calculated here do not correspond to actual form drag factors, because they depend on the mass of the iceberg. Thus, the optimal values reported here might be higher or lower than the actual values of the form drag factors. The optimized drag factors provide us with an interesting twist to our study. Can we estimate the iceberg mass

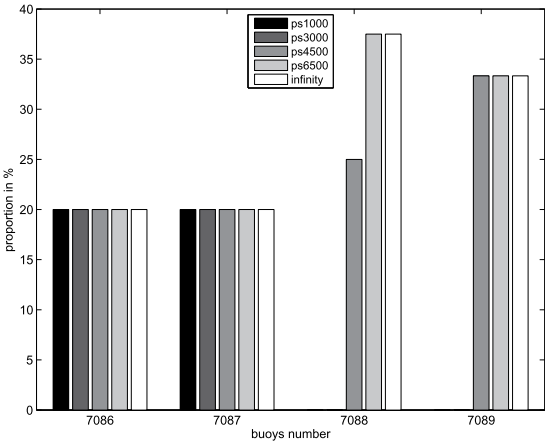

FIG. 8. For each observed iceberg, the proportion of modeled trajectories with different P_s threshold values among the successful simulations.

based on the actual drag coefficients and the optimized drag values retrieved in a manner similar to this study? This approach is theoretically feasible, although we question the practicality of this result, if for nothing else, then for the difficulty in calculating "correct" drag coefficients for a given iceberg.

The second experiment focused on the sea ice force parameterization defined in Eq. (6). We looked at the sensitivity of the threshold value P_s for our region of interest. The sea ice characteristics east of Svalbard in April–May 1990 did not have a direct impact on the iceberg trajectories. The ice flux from the central Arctic into the Barents Sea has strong interannual variations; therefore, it is possible that the parameterization may give better results for more severe ice years in the eastern Barents Sea.

In this study, we have tried to optimize some of the model parameters based on the relative importance of the forcing contributions. As in any model study, we depend on the accuracy of the forcing, which in this case is limited mainly by its spatial resolution. The bulk parameterization of the form and skin drag may also be too simple. Other force contributions, such as wake drag and wave radiation stress, are included implicitly through the variation of iceberg mass and drag force, albeit in a simplified form. A better parameterization of these mechanisms may improve our results.

Over a 2-month period, two of the icebergs are modeled with good accuracy, which illustrates that there is some skill in the system. Based on observed distributions of iceberg dimension, it is possible to estimate initial iceberg mass and corresponding form drag coefficients. In addition, including the thermodynamics will

allow for modeling long-term Barents Sea iceberg trajectories under different climate regimes. The optimal values of the iceberg mass and the drag coefficients have another property, which is appealing from a forecasting perspective. For ensemble data assimilation techniques such as the ensemble Kalman filter (Evensen 2007), the ensemble spread should be on the order of the forecast error, a property that the ''best model runs'' in Fig. 6 appear to have for icebergs 7088 and 7089. It is too early to speculate on the success of an ensemble-based iceberg forecasting system, but the results presented here are nonetheless encouraging.

Acknowledgments. The authors acknowledge Trond Mohn of Frank Mohn AS for a private endowment to the Mohn-Sverdrup Center. This work has also received partial funding from the MERSEA Integrated Project from the European Commission 6th Framework program and a grant computing time from the Norwegian Program for supercomputing (NOTUR). We thank F. Counillon for valuable discussion and comments on the study, and Michael Schodlock for sharing implementation details of the Alfred Wegener Institute iceberg drift model. We are also grateful to L. I. Eide and E. Nygaard from StatoilHydro ASA for providing the iceberg drift data.

REFERENCES

Abramov, V. A., 1992: Russian iceberg observations in the Barents Sea, 1933–1990. *Polar Res.,* **11,** 93–97.

Bentsen, M., G. Evensen, H. Drange, and A. D. Jenkins, 1999: Coordinate transformation on a sphere using conformal mapping. *Mon. Wea. Rev.,* **127,** 2733–2740.

Bertino, L., and K. A. Lisæter, 2008: The TOPAZ monitoring and prediction system for the Atlantic and Arctic Oceans. *J. Oper. Oceanogr.,* **2008** (2), 15–18.

Bigg, G. R., M. R. Wadley, D. P. Stevens, and J. A. Johnson, 1997: Modelling the dynamics and thermodynamics of icebergs. *Cold Reg. Sci. Technol.,* **26,** 113–135.

Bleck, R., 2002: An oceanic general circulation model framed in hybrid isopycnic-Cartesian coordinates. *Ocean Modell.,* **4,** 55–88.

Bourke, R., and R. Garrett, 1987: Sea ice thickness distribution in the Arctic Ocean. *Cold Reg. Sci. Technol.,* **13,** 259–280.

Browning, G. L., and H.-O. Kreiss, 1982: Initialization of the shallow water equations with open boundaries by bounded derivative method. *Tellus,* **34,** 334–351.

Drange, H., and K. Simonsen, 1996: Formulation of air–sea fluxes in ESOP2 version of MICOM. Tech. Rep. 125, Nansen Environmental and Remote Sensing Center, 23 pp.

Evensen, G., 2007: An ocean prediction system. *Data Assimilation: The Ensemble Kalman Filter,* Springer-Verlag, 231–237.

Hibler, W. D., 1979: A dynamic and thermodynamic sea ice model. *J. Phys. Oceanogr.,* **9,** 815–846.

Hunke, E. C., and J. K. Dukowicz, 1997: An elastic–viscous–plastic model for sea ice dynamics. *J. Phys. Oceanogr.,* **27,** 1849–1867.

Lichey, C., and H. H. Hellmer, 2001: Modeling giant-iceberg drift under the influence of sea ice in the Weddell Sea, Antarctica. *J. Glaciol.,* **47,** 452–460.

Løyning, T. B., 2001: Hydrography in the north-western Barents Sea, July–August 1996. *Polar Res.,* **20,** 1–11.

Lyard, F., F. Lefèvre, T. Letellier, and O. Francis, 2006: Modelling the global ocean tides: Modern insights from FES2004. *Ocean Dyn.,* **56,** 394–415.

Smith, S. D., 1993: Hindcasting iceberg drift using current profiles and winds. *Cold Reg. Sci. Technol.,* **22,** 33–45.

——, and E. G. Banke, 1983: The influence of the winds, currents and towing forces on the drift of icebergs. *Cold Reg. Sci. Technol.,* **6,** 241–255.

Sodhi, D. S., and M. El-Tahan, 1980: Prediction of an iceberg drift trajectory during a storm. *Ann. Glaciol.,* **1,** 77–82.

Spring, W., 1994: Ice data acquisition program: Summary report. Tech. Rep. File 472–37, Mobil Research and Development Corporation, Dallas E&P Engineering, 90 pp.

Svendsen, E., and Coauthors, 1983: Norwegian remote sensing experiment: Evaluation of the Nimbus 7 scanning multichannel microwave radiometer for sea ice research. *J. Geophys. Res.,* **88,** 2781–2792.

Teague, W., M. Carron, and P. Hogan, 1990: A comparison between the generalized digital environmental model and levitus climatologies. *J. Geophys. Res.,* **95,** 7167–7183.

Uppala, S. M., and Coauthors, 2005: The ERA-40 Re-Analysis. *Quart. J. Roy. Meteor. Soc.,* **131,** 2961–3012.